

Simulation of Flow Control in a Serpentine Duct

Onkar Sahni*

Joseph Olles†

Kenneth E. Jansen‡

Mechanical Aerospace and Nuclear Engineering, Rensselaer Polytechnic Institute, Troy, NY 12180, USA.

Three dimensional numerical computations of flow control within an aggressive serpentine inlet duct ($L/D = 1.5$) at a Mach number of $M = 0.45$ are presented. Two flow configurations including baseline flow (no flow control) and active flow control via steady, tangential control jet are considered. A stabilized finite element method is employed to perform turbulence simulations¹⁶ using two variants of the Spalart-Allmaras (S-A) model; the original S-A one-equation model²⁹ in an unsteady Reynold-averaged Navier-Stokes simulation (URANSS) and a hybrid S-A model³⁰ in a Detached eddy simulation (DES). Furthermore, computations are performed using adaptive meshing techniques developed for unstructured grids including boundary layer elements²⁴ to make such flow simulations practically feasible and efficient. Numerical results using two turbulence models are compared with experimental measurements³³ of static and total pressure for the baseline flow whereas numerical results based on URANSS and DES are compared in the case of flow control. Results obtained from URANSS using the original S-A model fail to predict key aspects of this complex flow with adverse pressure gradient and flow separation, whereas DES substantially improves the prediction.

I. Introduction

The inlet to an aircraft propulsion system is typically designed to supply flow to the compressor with minimal pressure loss, distortion or unsteadiness. Failure to do so can result in stall or surge of the compressor leading to reduced system performance or even catastrophic loss. Inlets often have increasing cross-sectional area to decelerate the flow at the compressor that lead to adverse stream-wise pressure gradients which in turn can result in separated flows. Moreover, inlets with short lengths and curvature are required for applications with constraints on packaging and low-observability, or overall size of the aircraft. Such short inlets give rise to cross-stream pressure gradients which cause secondary flows and separation. The combined effect of such flow features can result in a loss of total pressure as well as distortion at the aerodynamic interface plane (AIP), where the exit of inlet duct meets the compressor; diminishing the system performance. Therefore, flow control technologies based on passive and active techniques are applied to minimize the pressure loss, distortion and unsteadiness, and improve the system performance.

Baseline flow (with no flow control) in serpentine inlet or S-shaped ducts have been extensively studied both experimentally and numerically.^{10,19,34,35} Furthermore, many studies have been carried out to investigate the effectiveness of flow control in serpentine inlet ducts using both passive control techniques such as vortex generators,^{3,5,6,18,22} as well as active flow control based on steady or unsteady blowing or suction such as vortex generator jets or tangential control jets.^{4,26,31-33} Recently similar types of techniques have been applied and studied both experimentally and numerically for boundary-layer-ingesting (S-duct) inlets.^{1,2,11,12,20} In the current study, turbulence simulations are performed within an aggressive serpentine inlet duct by employing Streamline Upwind Petrov-Galerkin (SUPG) stabilized finite element formulation.¹⁶ Two variants of the Spalart-Allmaras (S-A) model are considered; the original S-A one-equation model²⁹ in an unsteady Reynolds-averaged Navier-Stokes simulation (URANSS) and a hybrid S-A model³⁰ in a

*Senior Research Associate, Member AIAA

†Graduate Student

‡Professor, Senior Member AIAA

Detached eddy simulation (DES). Furthermore, computations are performed using adaptive meshing techniques developed for unstructured grids including boundary layer elements²⁴ to make such flow simulations practically feasible and efficient.

II. Problem Setup

The serpentine inlet duct considered in this study has a very aggressive shape with length to exit height ratio, L/D , of 1.5, see Figure 1. The duct has a rectangular cross-section (114.3mm wide \times 88.9mm high)

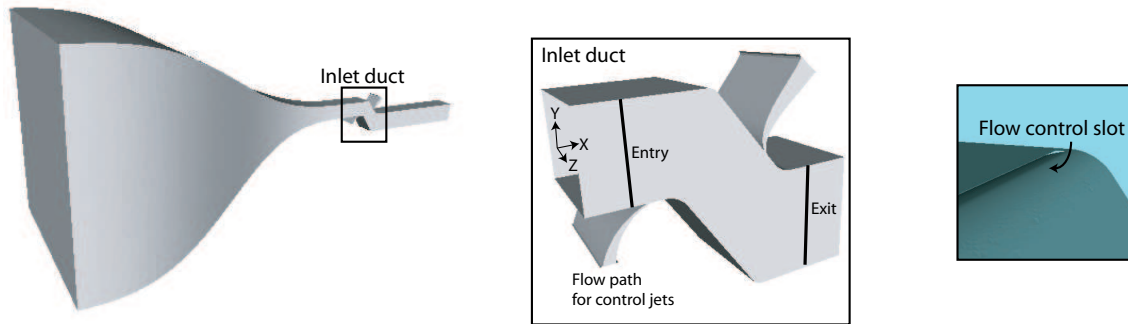


Figure 1. Geometry of the full computational domain including contraction, serpentine inlet duct and straight section with magnified views of the duct and the lower flow control slot.

at the entry and has a square cross-section (114.3mm wide \times 114.3mm high) at the exit (AIP), where $D = 114.3\text{mm}$. The offset between the two cross-sections of the duct is 101.6mm making the bottom wall at entry and top wall at exit lie on the same plane. For reference, center-point of the cross-section at the entry of the inlet duct is considered as the origin and the co-ordinate system is shown near the entry in Figure 1 (where x -axis is along the axial direction at the duct entry). In this study the computational domain incorporates a contraction section prior to the inlet duct to match the experimental setup and also includes a straight section after the exit of the duct, as shown in Figure 1.

Active flow control is considered by imposing steady, tangential control jet near the turn at the lower surface. Note that although there are two flow control sections present on turns at both the lower and upper surfaces, only the lower flow control jet is considered in this study. The jet enters the test section tangential to the surface through a rectangular slot that is 1mm in width and 101.6mm in span (leaving small capped portions symmetrically near both the side walls), see Figure 1.

The duct inlet Mach number of $M = 0.45$ is considered which is attained by prescribing a plug velocity profile and constant temperature at the entry of the contraction. A no-slip boundary condition is imposed at the walls that are assumed to be isothermal and static pressure is specific at the exit of the domain. In the case of flow control, a steady jet is applied by forcing 0.8% of the main flow through the lower flow control path resulting in steady (tangential) blowing prior to the turn at the lower surface of the duct.

III. Numerical Method

Two types of turbulence simulations are considered in this study; the original S-A one-equation model²⁹ in an unsteady Reynolds-averaged Navier-Stokes simulation and a hybrid S-A model³⁰ in a Detached eddy simulation. The resulting equations are discretized with a stabilized finite element method.¹⁶ The Streamline Upwind Petrov-Galerkin (SUPG) stabilized method is currently employed, which has been proven stable and higher order accurate (converging at the optimal rate for a given function space) for flows ranging from inviscid to viscous dominated.^{8,14,15}

The compressible Navier-Stokes equations (complete with continuity and total energy equations) are considered in the Favre-averaged form as

$$\mathbf{U}_{,t} + \mathbf{F}_{i,i}^{\text{adv}} - \mathbf{F}_{i,i}^{\text{diff}} = \mathcal{S} \quad (1)$$

where

$$\mathbf{U} = \begin{Bmatrix} U_1 \\ U_2 \\ U_3 \\ U_4 \\ U_5 \end{Bmatrix} = \bar{\rho} \begin{Bmatrix} 1 \\ \tilde{u}_1 \\ \tilde{u}_2 \\ \tilde{u}_3 \\ \tilde{e}_{\text{tot}} \end{Bmatrix}, \quad \mathbf{F}_i^{\text{adv}} = \tilde{u}_i \mathbf{U} + \bar{p} \begin{Bmatrix} 0 \\ \delta_{1i} \\ \delta_{2i} \\ \delta_{3i} \\ \tilde{u}_i \end{Bmatrix}, \quad \mathbf{F}_i^{\text{diff}} = \begin{Bmatrix} 0 \\ \tau_{1i} \\ \tau_{2i} \\ \tau_{3i} \\ \tau_{ij} \tilde{u}_j - q_i \end{Bmatrix} \quad (2)$$

and

$$\tau_{ij} = 2(\mu + \mu_T)(S_{ij}(\tilde{\mathbf{u}}) - \frac{1}{3}S_{kk}(\tilde{\mathbf{u}})\delta_{ij}), \quad S_{ij}(\tilde{\mathbf{u}}) = \frac{\tilde{u}_{i,j} + \tilde{u}_{j,i}}{2} \quad (3)$$

$$q_i = -(\kappa + \kappa_T)\tilde{T}_{,i}, \quad \kappa_T = c_p \frac{\mu_T}{Pr_T}, \quad \tilde{e}_{\text{tot}} = \tilde{e} + \frac{\tilde{u}_i \tilde{u}_i}{2}, \quad \tilde{e} = c_v \tilde{T} \quad (4)$$

where we use the overbar to denote an unweighted average and a tilde to denote a density weighted (Favre) average. The averaged variables are: the velocity \tilde{u}_i , the pressure \bar{p} , the density $\bar{\rho}$, the temperature \tilde{T} and the total energy \tilde{e}_{tot} . The constitutive laws relate the stress, τ_{ij} , to the deviatoric portion of the strain, $S_{ij}^d = S_{ij} - \frac{1}{3}S_{kk}\delta_{ij}$, through a molecular, μ , plus turbulent viscosity, μ_T . Similarly, the heat flux, q_i , is proportional to the gradient of temperature with the proportionality constant given by the addition of a molecular conductivity, κ , and a turbulent conductivity, κ_T , where the latter is assumed proportional to the turbulent viscosity as described above. While the formulation is not limited to an ideal gas, $\bar{p} = \bar{\rho}R\tilde{T}$, and constant specific heats at constant pressure, c_p , and at constant volume, c_v , that is the model used in this study. Furthermore, we have also assumed a constant molecular viscosity and constant conductivity through a constant Prandtl number. Finally \mathbf{S} is a body force (or source) term (in these studies equal to zero). This gives us the modeled form of the equations where the turbulent or eddy viscosity term requires modeling.

For the specification of the methods that follow, it is helpful to define the quasi-linear operator (with respect to a variable vector \mathbf{Y} to be defined later) related to (1) as

$$\mathcal{L} \equiv \mathbf{A}_0 \frac{\partial}{\partial t} + \mathbf{A}_i \frac{\partial}{\partial x_i} - \frac{\partial}{\partial x_i} (\mathbf{K}_{ij} \frac{\partial}{\partial x_j}) \quad (5)$$

from which \mathcal{L} can be naturally decomposed into time, advective, and diffusive portions

$$\mathcal{L} = \mathcal{L}_t + \mathcal{L}_{\text{adv}} + \mathcal{L}_{\text{diff}}. \quad (6)$$

Here $\mathbf{A}_i = \mathbf{F}_{i,\mathbf{Y}}^{\text{adv}}$ is the i^{th} Euler Jacobian matrix, \mathbf{K}_{ij} is the diffusivity matrix, defined such that $\mathbf{K}_{ij}\mathbf{Y}_{,j} = \mathbf{F}_i^{\text{diff}}$, and $\mathbf{A}_0 = \mathbf{U}_{,\mathbf{Y}}$ is the change of variables metric. For a complete description of $\mathbf{A}_0, \mathbf{A}_i$ and \mathbf{K}_{ij} , the reader is referred to literature.¹³ Using this, we can write (1) as simply $\mathcal{L}\mathbf{Y} = \mathbf{S}$.

To proceed with the finite element discretization of (1), we must precisely describe the approximation spaces with which we are dealing. First, let $\bar{\Omega} \subset \mathbf{R}^N$ represent the closure of the physical spatial domain (i.e. $\Omega \cup \Gamma$ where Γ is the boundary) in N dimensions, only $N = 3$ is considered here. In addition, $H^1(\Omega)$ represents the usual Sobolev space of functions with square-integrable values and derivatives on Ω .

Next, Ω is discretized into n_{el} finite elements, Ω^e . With this, we can define the trial solution space for the semi-discrete formulations as

$$\mathcal{V}_h = \{\mathbf{v}|\mathbf{v}(\cdot, t) \in H^1(\Omega)^m, t \in [0, T], \mathbf{v}|_{x \in \Omega^e} \in P_k(\Omega^e)^m, \mathbf{v}(\cdot, t) = \mathbf{g} \text{ on } \Gamma_g\}, \quad (7)$$

and the weighting function space as

$$\mathcal{W}_h = \{\mathbf{w}|\mathbf{w}(\cdot, t) \in H^1(\Omega)^m, t \in [0, T], \mathbf{w}|_{x \in \Omega^e} \in P_k(\Omega^e)^m, \mathbf{w}(\cdot, t) = \mathbf{0} \text{ on } \Gamma_g\}, \quad (8)$$

where $P_k(\Omega^e)$, is the space of all polynomials defined on Ω^e , complete to order $k \geq 1$, and m is the number of variables in the equation ($m = 5$).

To derive the weak form of (1), the entire equation is dotted from the left by a vector of weight functions, $\mathbf{W} \in \mathcal{W}_h$, and integrated over the spatial domain. Integration by parts is then performed to move the

spatial derivatives onto the weight functions (reducing the continuity requirements). This process leads to the integral equation (often referred to as the weak form): find $\mathbf{Y} \in \mathcal{V}_h$ such that

$$\begin{aligned}
0 &= \int_{\Omega} \left(\mathbf{W} \cdot \mathbf{U}_{,t} - \mathbf{W}_{,i} \cdot \mathbf{F}_i^{\text{adv}} + \mathbf{W}_{,i} \cdot \mathbf{F}_i^{\text{diff}} \right) d\Omega - \int_{\Gamma} \mathbf{W} \cdot \left(-\mathbf{F}_i^{\text{adv}} + \mathbf{F}_i^{\text{diff}} \right) n_i d\Gamma \\
&+ \sum_{e=1}^{n_{el}} \int_{\Omega^e} \mathcal{L}^T \mathbf{W} \cdot \boldsymbol{\tau} (\mathcal{L} \mathbf{Y} - \mathcal{S}) d\Omega
\end{aligned} \tag{9}$$

The first line of (9) contains the Galerkin approximation (interior and boundary) and the second line contains the least-squares stabilization. SUPG stabilization is obtained by replacing \mathcal{L}^T by $\mathcal{L}_{\text{adv}}^T$. The stabilization matrix $\boldsymbol{\tau}$ is an important ingredient in these methods and is well documented in literature.^{7,27} For current calculations, variable vector \mathbf{Y} is chosen to be pressure-primitive variables (e.g., $\mathbf{Y}^T = \{p, u, v, w, T\}$).

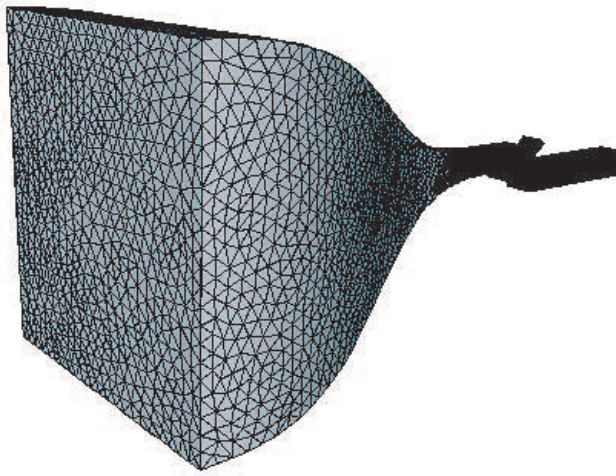
To develop a numerical method, the weight functions (\mathbf{W}), the solution variable (\mathbf{Y}), and it's time derivative ($\mathbf{Y}_{,t}$) are expanded in terms of basis functions (typically piecewise polynomials; all calculations described herein were performed with linear basis). The integrals (9) are then evaluated numerically using Gauss quadrature resulting in a system of non-linear ordinary differential equations. The system of non-linear ordinary differential equations obtained is discretized in time via a second-order generalized- α time integrator¹⁷ resulting in a non-linear system of algebraic equations. The non-linear system of algebraic equations obtained is in turn linearized with Newton's method which yields a linear algebraic system of equations. The GMRES method,²³ with sparse storage and a block-diagonal pre-conditioner, is used to solve the linear system of equations. Note that the one-equation S-A model is a scalar analog of the Navier-Stokes equations and can therefore follow the same steps described in (1) through (9) with \mathbf{Y} replaced by the S-A eddy viscosity variable. Then, the vector and scalar system corresponding to the averaged Navier-Stokes and S-A eddy viscosity equations are solved in a staggered form to achieve non-linear convergence of the combined equations at every time step.

IV. Adaptive meshing

An inherent property of all numerical methods employed to simulate physical phenomenon by discretizing a set of governing equations on a physical domain is that the solution obtained is an approximate one and thus, possesses error. For practical problems of interest, a prior determination of such errors is often not feasible as local discretization errors are significantly influenced by the solution features of the problem whose knowledge is typically limited or not available. In this scenario, an effective way to control the discretization error is to estimate it, by using *a posteriori* measures, on the current discretization and reduce it by iteratively improving the discretization. In this study we employ adaptive meshing techniques developed for unstructured grids including boundary layer elements to make such flow simulations practically feasible and efficient. To carry out the adaptive mesh-based flow simulations we perform the flow computations and evaluate the quality of the computed solution on the current mesh to determine its suitability. These error indicators can also be combined with flow feature identification to concentrate early adaptivity on regions known to be important. For example, we currently use pressure loss as an indicator to determine the presence of flow features such as separation and secondary flows, and to improve the mesh resolution locally in these regions. The adaptive techniques used in this study are capable of maintaining the layered structure present in such meshes near the walls due to presence of boundary layer elements²⁴ that are critical for viscous flow simulations.²⁵

The initial, unstructured mesh containing boundary layer elements near the walls is shown in Figure 2. Such a mesh is commonly referred to as boundary layer mesh (or semi-structured mesh)^{9,21} and maintains desirable attributes for viscous flow simulations due to use of high-aspect ratio, orthogonal, layered and graded elements near the walls. Care is taken to produce elements of acceptable shape at turns and corners within the domain; and also to ensure a smooth transition between the layered part and the interior tetrahedral part of the mesh as can be seen in Figure 2 from the interior mesh faces near the fillet at the lower flow control slot. Moreover, use of completely unstructured tetrahedral elements elsewhere in the the interior of the domain allows for significant but smooth (graded) variation of local mesh resolution making simulations practically feasible. In the current mesh, for example, length of mesh-edges in the contraction section is about $h = D/2$, whereas mesh-edges near the flow control slots are of length $h = D/2000$ ($= 0.05715mm$); resulting in a change of local mesh resolution by three orders of magnitude. Also note that the length of

Surface mesh of the full domain



Surface and interior mesh faces near the lower flow control slot

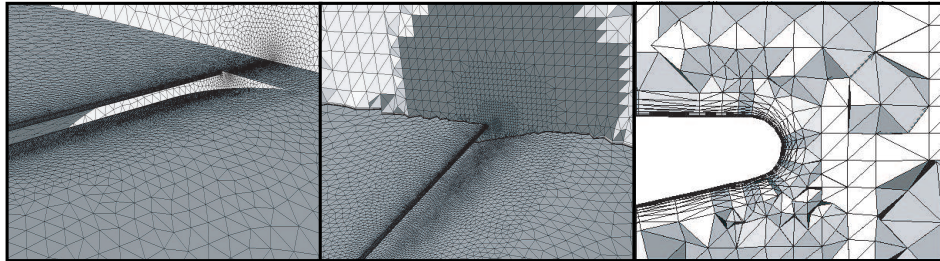


Figure 2. Mesh of the full computational domain along with magnified views of surface mesh and interior mesh faces near the lower flow control slot.

mesh-edges at the central core of the inlet duct is $h = D/20$ (including portions around the vertical planes passing through the flow control slots), leading to variation of mesh resolution by a factor of 100 as compared to mesh-edges near the flow control slots. This initial distribution of mesh sizes is based on preliminary insight but it is important to point out that the precise resolution needs of flow in such a complicated geometry cannot be fully defined prior to the simulation. Therefore, such initial meshes are constructed to allow the use of mesh adaptivity for subsequent more resolved simulations, where the mesh resolution can be changed (locally) based on the quality of the computed solution features. Use of such techniques in turn allows for efficient simulations of real-life problems by focusing mesh resolution in regions of interest. Figure 3 shows the initial and adapted boundary layer meshes used in the current study (meshes contain about 2.5 and 4 million points, respectively). It is clear that the adapted mesh contains finer resolution only in specific portions after both the turns in the inlet duct which is due to the presence of flow separation and secondary flows (that are shown in the next section on results). In the first phase of adaptivity within layered elements in this study, only the in-plane resolution of boundary layer elements was adapted while the thickness of the layered elements was held fixed at y^+ values that maintained the first grid points off the walls at order 1 or lower in the baseline flow case.

V. Results

In this section, we present the numerical results obtained using two turbulence models for both the flow configurations: baseline case (no flow control) and flow control case with 0.8% steady blowing through the lower slot. In the baseline case, numerical results based on URANSS and DES are compared with the experimental measurements of static and total pressure. Experimental measurements were not available for the lower flow control case of 0.8% steady blowing. In all cases, the time step size was fixed to a value of $6.125\mu\text{sec}$, leading to 180 steps per inlet-duct flight-time based on the centerline velocity at the entry

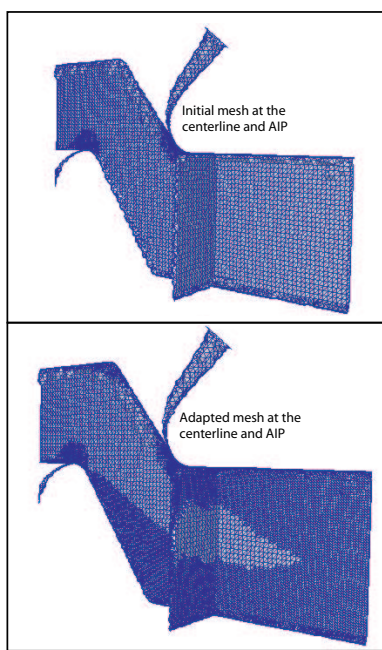


Figure 3. Initial and adapted meshes (near the inlet duct) at the centerline and AIP.

of the duct and length of the inlet (entry to AIP). The results presented here are based on the average quantities computed using 200 samples equally distributed over 10,000 time steps or about 56 flight-times. Average quantities using 1000 samples over the same time interval produced similar results with insignificant differences. Considering samples in half of the physical time interval also led to insignificant differences. In terms of computational resources, simulations on the refined mesh were performed using 1024 processors at a rate of about one flight-time per hour (computations in this study were carried out on the Ranger system at the Texas Advanced Computing Center and Opteron Blade Cluster at the Computational Center for Nanotechnology Innovations). Note that the current analysis code (PHASTA) has been shown to scale at $O(10^4)$ processors.²⁸

V.A. Static pressure distribution

The static pressure distribution is presented in the form of pressure coefficient: $C_p = (p - p^{wall}) / (p_0^{in} - p^{wall})$ (where, p is the local static pressure, p^{wall} is the reference static pressure taken as average of static pressure values at the center of four walls near the entry of the duct and p_0^{in} is the reference total pressure taken at the main inlet or entry of the contraction section; these reference values are selected to be consistent with the experimental measurements). The pressure coefficient for both the baseline and flow control cases at the lower surface along centerline and off-centerline (44.45mm) are presented in Figure 4. It is clear from the baseline flow case that the DES predictions are in much better agreement with the experimental measurements than the URANSS, especially at the centerline. URANSS predicts much higher values of pressure coefficient at the centerline for this case (for $x/D > 1$). For the flow control case the differences between URANSS and DES are relatively smaller. Figure 4 also shows that in both cases the flow is separated downstream of the first turn on the lower surface and re-attaches near the second turn. Based on simulation results, this particular flow control case shows marginal improvement in controlling the flow separation.

V.B. Total pressure distribution

The total pressure distribution is presented in the form of pressure recovery defined as: $PR = p_0 / p_0^{in}$ (where, p_0 is the local total pressure and as before, p_0^{in} is the reference total pressure taken at the entry of the contraction section). Pressure recovery values at the AIP plane along centerline and off-centerline (25.4mm) for both baseline and flow control cases are presented in Figure 5. Similar to predictions of static pressure coefficient, pressure recovery values obtained through DES are in much better agreement with the

experimental measurements than those of the URANSS. Again, URANSS predicts much higher pressure values at the centerline.

Figure 5 also indicates the presence of secondary flows near the lower wall. Figure 6 provides further insight, where pressure recovery results from URANSS and DES are shown at the centerline and AIP. In the case of URANSS, relatively large and stable vortices are predicted at the lower corners that can be seen at the AIP. These corner vortices in the case of URANSS pull the flow down at the centerline leading to the prediction of higher centerline values of pressure recovery, and also pressure coefficient, which is in disagreement with the experimental measurements. As before, simulation results show that this particular level of flow control provides marginal improvement in pressure recovery at the centerline whereas it is ineffective at the off-centerline location.

V.C. Instantaneous flow field

The results presented thus far are time-averaged results of unsteady simulations. To get a sense of the unsteadiness present in the flow, Figure 7 shows instantaneous Mach number for both baseline and flow control cases at the centerline and AIP that are obtained through URANSS and DES. URANSS captures some unsteadiness but, as expected, the large eddy viscosity field smears the smaller flow structures and predicts separation that is relatively shorter (especially at the centerline). DES resolves much more unsteadiness and smaller flow structures leading to an improved prediction as seen in static pressure coefficient and pressure recovery, refer Figures 4 and 5. To get a three dimensional perspective of this unsteadiness, isosurfaces of the spanwise velocity at an instant for the baseline flow are shown in Figure 8. The long, tubular structures in the URANSS solution are the results of the relatively strong corner vortices. The smaller, more unsteady, structures present in the DES appear to disrupt the formation or otherwise breakup the large corner vortices that caused the URANSS model to give a poor prediction. Further mesh refinement cycles are necessary to confirm this hypothesis. While Figures 7 and 8 show particular instants, they are representative with only modest variation in the URANSS case from this stable vortical structure and high variation in the DES case.

VI. Conclusion

Turbulence simulations in an aggressive serpentine inlet duct ($L/D = 1.5$) with and without flow control are performed. A stabilized finite element method along with adaptive meshing techniques are employed to make such simulations practically feasible and efficient. Two variants of the Spalart-Allmaras (S-A) model are considered; the original S-A one-equation model in URANSS and a hybrid S-A model in DES. Numerical results obtained through URANSS and DES are compared with experimental measurements of static and total pressure for the baseline flow. Values predicted by DES are in good agreement with the experiments whereas URANSS prediction is poor. Simulation results show that the effects of flow control based on 0.8% steady blowing through the lower slot are marginal. Significant effort is still required to improve the modeling of such flows including additional mesh refinement.

Acknowledgments

Dr. Michael Amitay and John Vaccaro provided valuable discussions along with experimental data for the baseline flow case. Computing resources were provided in part by the NSF through TeraGrid resources at Texas Advanced Computing Center (Ranger and Spur systems were used) and by Rensselaer's Computational Center for Nanotechnology Innovations which was funded by the State of New York, IBM and Rensselaer Polytechnic Institute. This work is supported in part by NSF under grant OCI-0749152. The results presented in this article made use of the linear algebra library provided by ACUSIM Software Inc. We would also like to acknowledge that we made use of Paraview software provided by Kitware Inc. for data visualization.

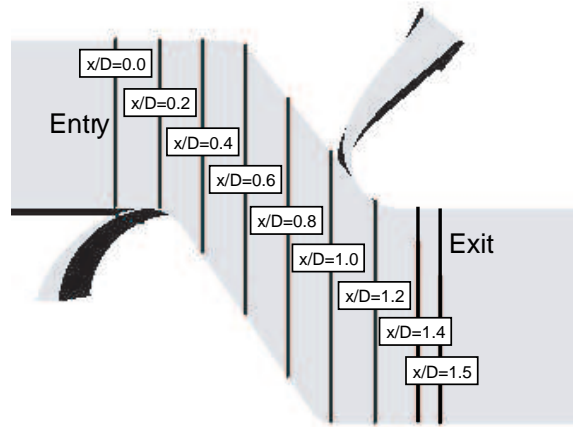
References

- ¹B.G. Allan and L.R. Owens. Numerical modeling of flow control in a boundary-layer-ingesting offset inlet diffuser at transonic Mach numbers. In *44th AIAA Aerospace Sciences Meeting and Exhibit*, Reno, NV, Jan. 2006. AIAA-2006-845.
- ²A.J. Anabtawi, R.F. Blackwelder, P.B.S. Lissaman, and R.H. Liebeck. An experimental investigation of boundary layer

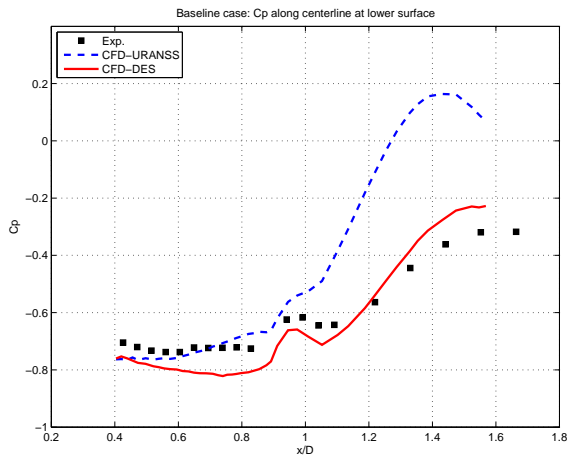
- ingestion in a diffusing S-duct with and without passive flow control. In *37th AIAA Aerospace Sciences Meeting and Exhibit*, Reno, NV, Jan. 1999. AIAA-1999-739.
- ³B.H. Anderson and J. Gibb. Study on vortex generator flow control for the management of inlet distortion. *J. of Propulsion and Power*, 9(3):422–430, 1993.
- ⁴B.H. Anderson, D.N. Miller, G.A. Addington, and J. Agrell. Optimal micro-jet flow control for compact air vehicle inlets. *Technical Memorandum*, NASA/TM-2004-212937, 2004.
- ⁵B.H. Anderson, D.N. Miller, G.A. Addington, and J. Agrell. Optimal micro-vane flow control for compact air vehicle inlets. *Technical Memorandum*, NASA/TM-2004-212936, 2004.
- ⁶J.C. Dudek. An empirical model for vane-type vortex generators in a Navier-Stokes code. In *43rd AIAA Aerospace Sciences Meeting and Exhibit*, Reno, NV, Jan. 2005. AIAA-2005-1003.
- ⁷L. P. Franca and S. Frey. Stabilized finite element methods: II. The incompressible Navier-Stokes equations. *Comp. Meth. Appl. Mech. Engng.*, 99:209–233, 1992.
- ⁸L. P. Franca and T. J. R. Hughes. Convergence analyses of Galerkin / least-squares methods for symmetric advective-diffusive forms of the Stokes and incompressible Navier-Stokes equations. *Comp. Meth. Appl. Mech. Engng.*, 105:285–298, 1993.
- ⁹R. V. Garimella and M. S. Shephard. Boundary layer mesh generation for viscous flow simulations. *Int. J. Numer. Meth. Engng.*, 49:193–218, 2000.
- ¹⁰G.J. Harloff, B.A. Reichert, and S.R. Wellborn. Navier-Stokes analysis and experimental data comparison of compressible flow in a diffusing S-duct. In *10th AIAA Applied Aerodynamics Conference*, Palo Alto, CA, June 1992. AIAA-1992-2699.
- ¹¹N.A. Harrison, J. Anderson, J.L. Fleming, and W.F. Ng. Computational analysis of active flow control of a boundary layer ingesting serpentine inlet diffuser. In *44th AIAA Aerospace Sciences Meeting and Exhibit*, Reno, NV, Jan. 2006. AIAA-2006-874.
- ¹²N.A. Harrison, J. Anderson, J.L. Fleming, and W.F. Ng. Experimental investigation of active flow control of a boundary layer ingesting serpentine inlet diffuser. In *45th AIAA Aerospace Sciences Meeting and Exhibit*, Reno, NV, Jan. 2007. AIAA-2007-843.
- ¹³G. Hauke. *A unified approach to compressible and incompressible flows and a new entropy-consistent formulation of the $k-\epsilon$ model*. PhD thesis, Stanford University, 1995.
- ¹⁴T. J. R. Hughes, L. P. Franca, and G. M. Hulbert. A new finite element formulation for fluid dynamics: VIII. The Galerkin / least-squares method for advective-diffusive equations. *Comp. Meth. Appl. Mech. Engng.*, 73:173–189, 1989.
- ¹⁵T. J. R. Hughes, L. P. Franca, and M. Mallet. A new finite element formulation for fluid dynamics: VI. Convergence analysis of the generalized SUPG formulation for linear time-dependent multidimensional advective-diffusive systems. *Comp. Meth. Appl. Mech. Engng.*, 63:97–112, 1987.
- ¹⁶K. E. Jansen. A stabilized finite element method for computing turbulence. *Comp. Meth. Appl. Mech. Engng.*, 174:299–317, 1999.
- ¹⁷K. E. Jansen, C. H. Whiting, and G. M. Hulbert. A generalized- α method for integrating the filtered Navier-Stokes equations with a stabilized finite element method. *Comp. Meth. Appl. Mech. Engng.*, 190:305–319, 1999.
- ¹⁸A. Jirasek. Design of vortex generator flow control in inlets. *J. of Aircraft*, 43(6):1886–1892, 2006.
- ¹⁹A. Kirk, A. Kumar, J. Gargoloff, O. Rediniotis, and P. Cizmas. Numerical and experimental investigations of a serpentine inlet duct. In *45th AIAA Aerospace Sciences Meeting and Exhibit*, Reno, NV, Jan. 2007. AIAA-2007-842.
- ²⁰V. Kumar and F.S. Alvi. Efficient control of separation using microjets. In *35th AIAA Fluid Dynamics Conference and Exhibit*, Toronto, ON, June 2005. AIAA-2005-4879.
- ²¹S. Pirzadeh. Unstructured viscous grid generation by the advancing-layers method. *AIAA Journal*, 32:1735–1737, 1994.
- ²²B.A. Reichert and B.J. Wendt. Improving diffusing S-duct performance by secondary flow control. In *32nd AIAA Aerospace Sciences Meeting and Exhibit*, Reno, NV, Jan. 1994. AIAA-1994-365.
- ²³Y. Saad and M.H. Schultz. GMRES: A generalized minimal residual algorithm for solving nonsymmetric linear systems. *SIAM J. of Sc. and Stat. Comput.*, 7:856–869, 1986.
- ²⁴O. Sahni, K.E. Jansen, M.S. Shephard, C.A. Taylor, and M.W. Beall. Adaptive boundary layer meshing for viscous flow simulations. *Engng. with Comp.*, 24(3):267–285, 2008.
- ²⁵O. Sahni, J. Mueller, K.E. Jansen, M.S. Shephard, and C.A. Taylor. Efficient anisotropic adaptive discretization of cardiovascular system. *Comp. Meth. Appl. Mech. Engng.*, 195(41-43):5634–5655, 2006.
- ²⁶A.R. Scribber, W. Ng, and R. Burdisso. Effectiveness of a serpentine inlet duct flow control technique at design and off-design simulated flight conditions. *J. of Turbomachinery*, 128(2):332–339, 2006.
- ²⁷F. Shakib. *Finite element analysis of the compressible Euler and Navier-Stokes equations*. PhD thesis, Stanford University, 1989.
- ²⁸M.S. Shephard, K.E. Jansen, O. Sahni, and L.A. Diachin. Parallel adaptive simulations on unstructured meshes. *Journal of Physics: Conference Series*, 78(012053), 2007.
- ²⁹P.R. Spalart and S.R. Allmaras. A one-equation turbulence model for aerodynamic flows. In *30th AIAA Aerospace Sciences Meeting and Exhibit*, Reno, NV, Jan. 1992. AIAA-1992-439.
- ³⁰P.R. Spalart, W.H. Jou, M. Strelets, and S.R. Allmaras. Comments on the feasibility of LES for wings and on a hybrid RANS/LES approach. In *Advances in DNS/LES*, pages 137–147, Columbus, OH, 1997. Greyden Press.
- ³¹R.K. Sullerey, V.S. Mangat, and A. Padhi. Flow control in serpentine inlet using vortex generator jets. In *3rd AIAA Flow Control Conference*, San Francisco, CA, June 2006. AIAA-2006-3499.
- ³²S.E. Tournier, J.D. Paduano, and D. Pagan. Flow analysis and control in a transonic inlet. In *23rd AIAA Applied Aerodynamics Conference*, Toronto, ON, June 2005. AIAA-2005-4734.
- ³³J. Vaccaro, J. Vasile, and M. Amitay. Active control of inlet ducts. In *26th AIAA Applied Aerodynamics Conference*, Honolulu, HI, Aug. 2008. AIAA-2008-6402.

³⁴A. Vakili, J.M. Wu, W.R. Hingst, and C.E. Towne. Comparison of experimental and computational compressible flow in a S-duct. In *22nd AIAA Aerospace Sciences Meeting and Exhibit*, Reno, NV, Jan. 1984. AIAA-1984-33.

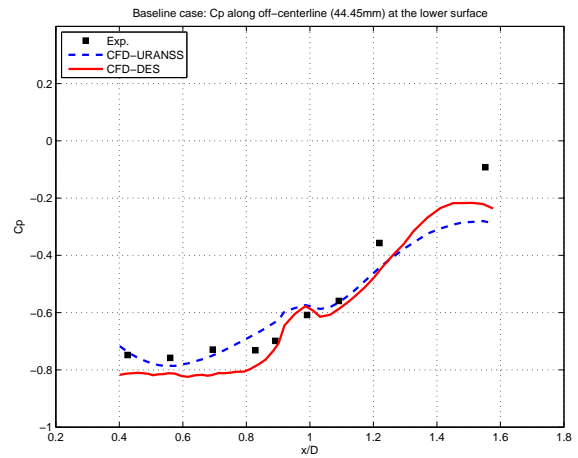
³⁵S.R. Wellborn, B.A. Reichert, and T.H. Okiishi. An experimental investigation of the flow in a diffusing S-duct. In *28th AIAA/ASME/SAE/ASEE Joint Propulsion Conference and Exhibit*, Nashville, TN, July 1992. AIAA-1992-3622.



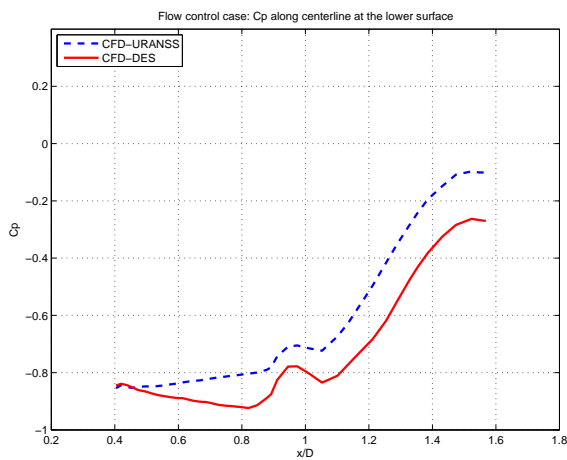
(a) Reference for x/D values



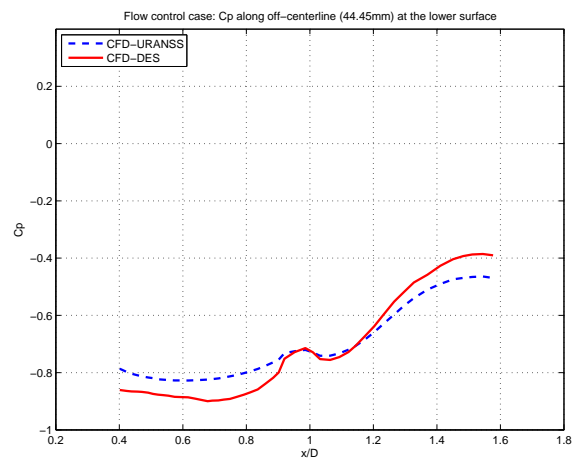
(b) Baseline case: C_p at centerline



(c) Baseline case: C_p at off-centerline

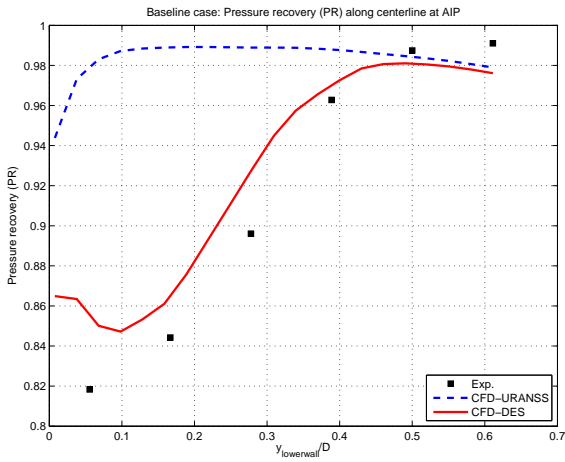


(d) Flow control case: C_p at centerline

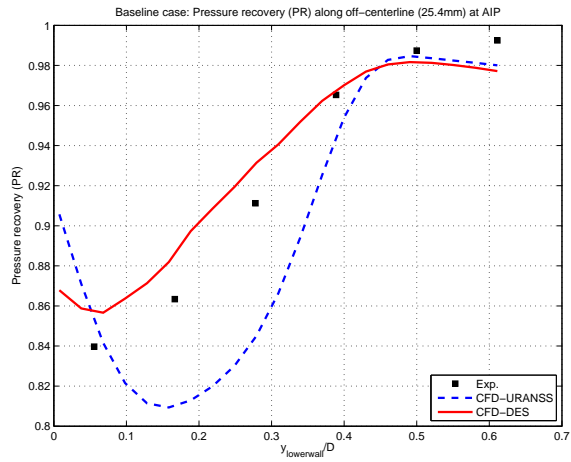


(e) Flow control case: C_p at off-centerline

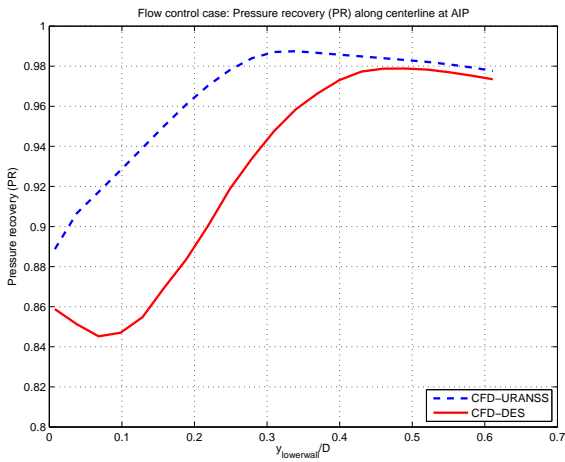
Figure 4. Pressure coefficient (C_p) distribution for both baseline and flow control cases at the lower surface along centerline and off-centerline (44.45mm).



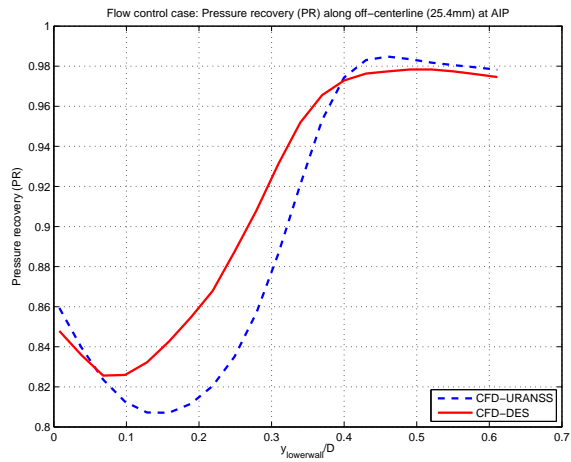
(a) Baseline case: PR at centerline



(b) Baseline case: PR at off-centerline

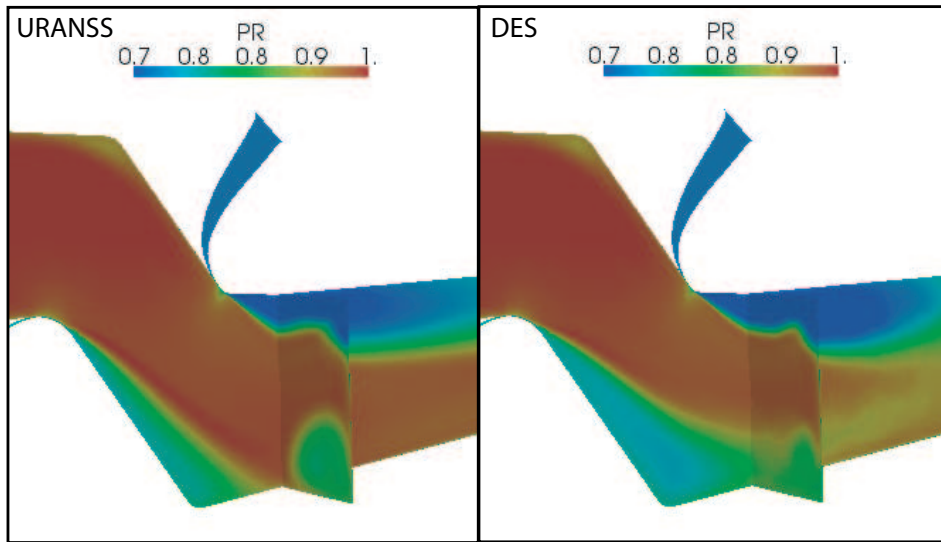


(c) Flow control case: PR at centerline

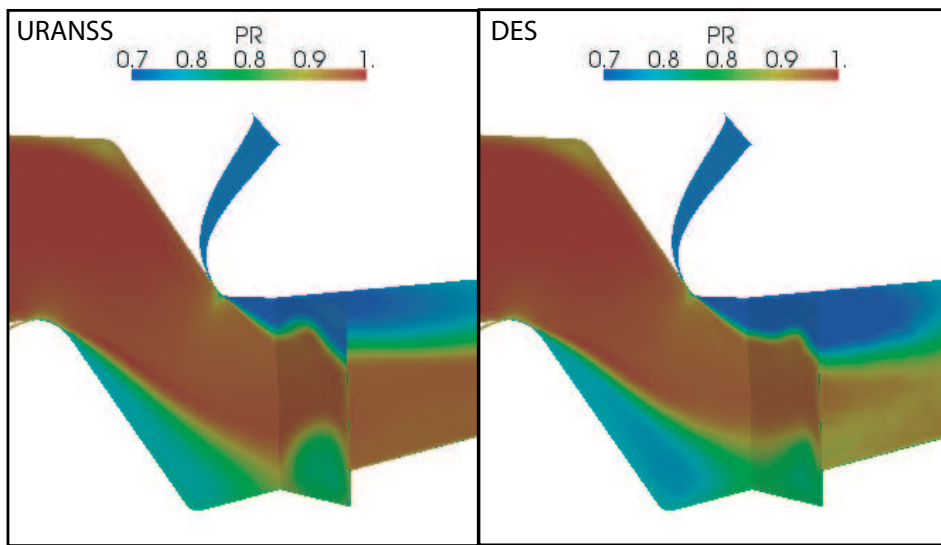


(d) Flow control case: PR at off-centerline

Figure 5. Pressure recovery distribution for both baseline and flow control cases at the AIP plane along centerline and off-centerline (25.4mm) (where, $y_{lowerwall}$ is the vertical distance from the lower surface/wall and $y_{lowerwall}/D = 0.5$ is in the middle of upper and lower walls).

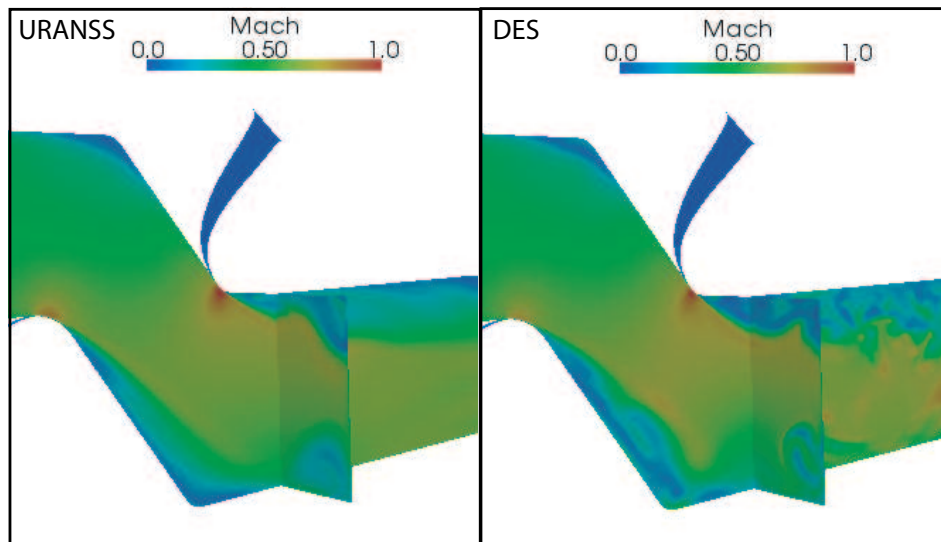


(a) Baseline case: PR at centerline and AIP

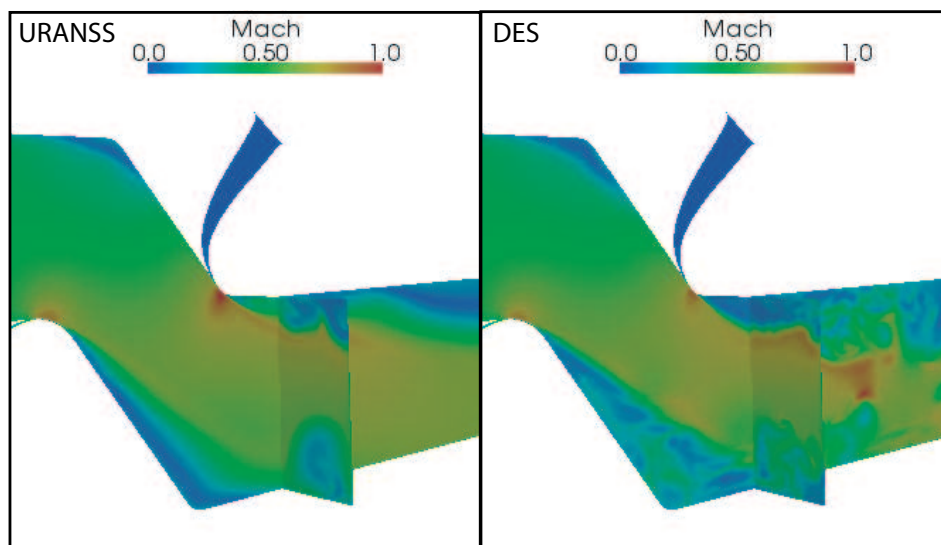


(b) Flow control case: PR at centerline and AIP

Figure 6. Pressure recovery field for both baseline and flow control cases at the centerline and AIP based on URANSS and DES.



(a) Baseline case: Snapshot of Mach number at centerline and AIP



(b) Flow control case: Snapshot of Mach number at centerline and AIP

Figure 7. Snapshot of Mach number for both baseline and flow control cases at the centerline and AIP based on URANSS and DES.

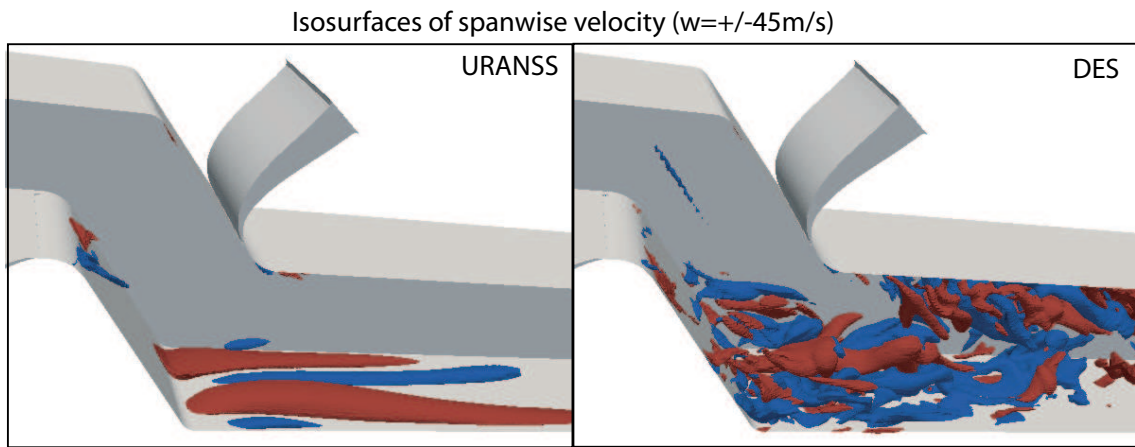


Figure 8. Isosurfaces of spanwise velocity ($w = \pm 45 \text{ m/s}$) at an instant for baseline flow case based on URANSS and DES.